ORIGINAL PAPER

Spectral discrimination of Recent sediments around Bhuj, India, using Landsat-TM data and assessment of their vulnerability to seismicity-related failures

D. Ramakrishnan

Abstract   Kachchh region of India is a rift basin filled with sediments from Jurassic to Quaternary ages. This area is tectonically active and witnessed several major earthquakes since the recent historical past. During an earthquake event, the water-laden foundation soil liquefies and causes damage to buildings and other civil engineering structures. The January 26, 2001, Bhuj earthquake demonstrated extensive liquefaction-related damages in entire Kachchh Peninsula. Therefore, evaluation of liquefaction susceptibility of unconsolidated sediments is a vital requirement for developing seismic microzonation maps. In this paper, a new approach involving remote sensing techniques and geotechnical procedures is demonstrated for effective mapping of liquefaction-susceptible areas. The present and paleo-alluvial areas representing unconsolidated sediments were mapped using Landsat-TM data and field reflectance spectra. Spectral discrimination of alluvial area was made using the feature-oriented principal component selection and spectral angle mapping techniques. Subsequently, field geotechnical investigations were carried out in these areas. It is evident from the results that the alluvial soils are predominantly sandy loam with very low (7–28) standard penetration test values. The evaluated factor of safety for these soils varies from 0.43 to 1.7 for a peak ground acceleration of 0.38. Finally, a liquefaction susceptibility map is prepared by integrating results on alluvium distribution, factor of safety, and depth to water table.

Keywords   Ground deformation · Seismicity · Factor of safety · Hazard vulnerability · Spectral remote sensing · GIS

1 Introduction

Liquefaction, the process of sudden loss of soil strength due to seismic loading, is a cause of concern in most of the active tectonic regions. Alluvial terrene characterized

D. Ramakrishnan (✉)
Department of Earth Sciences, Indian Institute of Technology Bombay, Mumbai 400 076, India
e-mail: ramakrish@iitb.ac.in

by unconsolidated, saturated sediments is vulnerable to liquefaction-related ground failures, such as lateral and vertical displacement, and settlement. These failures damage civil engineering structures and result in extensive human and property loss (Ishihara 1993; Chu et al. 2003; Leea et al. 2003; Haiming et al. 2004; Franck et al. 2005). Testimony to such devastation is widely recorded in events such as Northridge (Thomas et al. 1999), Chi-Chi (Yuan et al. 2003), Kashmir (Sahoo et al. 2007), Chile (Verdugo et al. 2012), and New Zealand (Orense et al. 2012). Hence, liquefaction potential assessment of foundation soil is one of the important criteria in preparing seismic microzonation maps (Youd 1991). This involves mapping the aerial distribution of unconsolidated sediments (Youd and Keefer 1981) and estimation of the seismic demand imposed by an earthquake to the soil's resistance to generate excess pore pressure (Youd and Perkins 1987).

For spatial mapping of alluvial areas, optical and microwave remote sensing techniques have been gaining importance (e.g., Gupta et al. 1998; Singh et al. 2001; Saraf et al. 2002; Saito et al. 2004; Oommen and Baise 2008; Ishitsuka et al. 2012). Once the vulnerable areas are delineated, field- and laboratory-based geotechnical investigations are carried out to evaluate the liquefaction potential. Some of the standard techniques developed to evaluate seismic demand include cyclic stress method (Seed and Idriss 1971; Whitman 1971), the cyclic strain method (Dobry et al. 1982), and energy-based methods (Davis and Berrill 1982; Kayen and Mitchell 1997; Green and Mitchell 2004).

Kachchh Peninsula, Gujarat, India, has witnessed several devastating earthquakes since the historical past (Rajendran et al. 2001). During the latest event (January 26, 2001, Mw 7.7), extensive liquefaction-related damages were reported in the entire peninsula (Tuttle and Hengesh 2002; Iyengar and Raghukanth 2002; Krinitzsky and Hynes 2002; Singh et al. 2005; Ramakrishnan et al. 2006). Hence, this area warrants a detailed liquefaction susceptibility/vulnerability map. In this work, an attempt is made to prepare a liquefaction susceptibility map for Bhuj city and the surrounding areas based on the inputs from remote sensing and field geotechnical studies. The procedures adopted include (1) delineation of alluvial areas based on field- and satellite reflectance spectra, (2) field survey for groundwater conditions and past episodes of ground failures, (3) geotechnical investigations, and (4) data integration, analyses, and generation of liquefaction susceptibility map using geographic information system (GIS).

2 Geology and seismotectonics of Kachchh

Kachchh Peninsula (Fig. 1) forms the westernmost part of the Indian subcontinent. Kachchh seismotectonic belt extends approximately 250 km (east–west) and 150 km (north–south). It is flanked between Nagar Parkar Fault in north and Kathiawar Fault in south. The area in between is traversed by several fault systems. Salient among them are Katrol Hill Fault (KHF), Kachchh Mainland Fault (KMF), Banni Fault (BF), Island Belt Fault (IBF), and Allah Bund Fault (ABF). Geologically, Kachchh region comprises predominantly sedimentary rocks of Mesozoic (sandstone, siltstone, shale, and limestone), Tertiary (poorly consolidated sandstone, siltstone, and clay), and Quaternary (sand and clay) periods. The unconsolidated sediments are often associated with present/paleo-channels, young and older alluvial plains, alluvial fans, and mudflats.
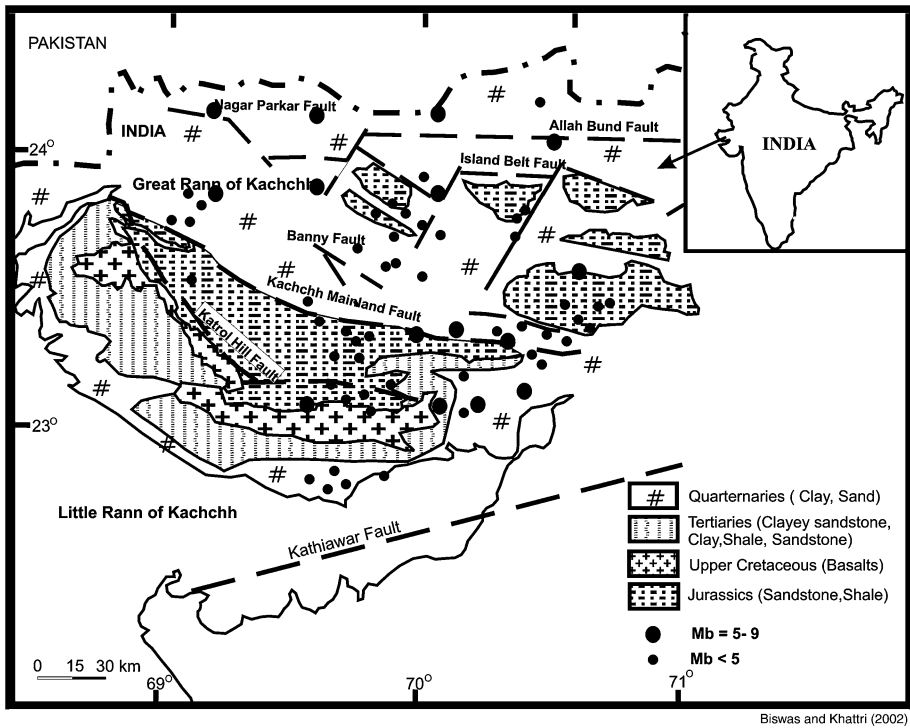
Fig. 1 Geology and seismotectonic setup of Kachchh Peninsula

3 Methodology

3.1 Data processing and image analysis

In this study, Landsat-TM7 satellite data is used to map the alluvial areas. This freely available data (www.glcf.umd.edu) has adequate spectral bands to delineate the constituent minerals of alluvial soils, such as quartz, hydroxyl mineral assemblages (kaolin, montmorillonite, illite, and chlorite), and iron hydroxides (goethite, boehmite) (Abrams et al. 1983; Buckingham and Sommer 1983; Amos and Greenbaum 1989; Kaufman 1988; Tangestani and Moore 2001).

Landsat data (path 150, row 44) was analyzed using the ERDAS-Imagine (ver. 8.7) and ENVI (ver. 4.3) software. The satellite imagery was geo-corrected using World Geodetic System (WGS-84) as reference and Universal Transverse Mercator (UTM) as projection system. For this purpose, 50 ground control points (GCP) collected using a Global Position System (GPS) were used in conjunction with a nonparametric (second-order polynomial fit) model. From the digital numbers (DN) of satellite data, surface apparent reflectance values for bands 1, 2, 3, 4, 5, and 7 were computed following the methods of Van der Meer et al. (1997) and Chander and Markham (2003). This involves (1) dequantization and conversion from calibrated DN to at-sensor radiance for each band using Eq. 1, (2) estimation of top of atmosphere (TOA) reflectance using Eq. 2, and (3) calculation of at-surface apparent reflectance by invariant object method (Liang 2001):

$$L_\lambda = \left(\frac{LMAX_\lambda - LMIN_\lambda}{Q_{Calmax}}\right)Q_{Cal} + LMIN_\lambda \qquad (1)$$

where L_λ represents at-sensor spectral radiance (W/(m^2.sr.µm)), Q_{cal} quantized calibrated pixel value (0–255), Q_{calmin} minimum quantized calibrated pixel value (DN = 0) corresponding to $LMIN_\lambda$, Q_{calmax} maximum quantized pixel value (DN = 255) corresponding to $LMAX_\lambda$, $LMIN_\lambda$ spectral radiance that is scaled to Q_{calmin} (W/(m^2.sr.µm)), and $LMAX_\lambda$ spectral radiance that is scaled to Q_{calmax} (W/(m^2.sr.µm)).

$$\rho_p = \frac{\pi * L_\lambda * d^2}{ESUN_\lambda * Cos\varphi} \qquad (2)$$

where ρ_p—at-sensor reflectance, d—Earth–Sun distance, $ESUN_\lambda$—mean solar irradiance, and φ—solar zenith angle.

Transformation of at-sensor reflectance to apparent ground reflectance was carried out using the flat field normalization algorithm (Chavez 1996) embedded in ENVI software. For this purpose, average reflectance of sandy exposures (invariant objects) occurring within the image was used.

Using the reflectance image, two different approaches were carried out to delineate the alluvial areas. The first approach involved performing feature-oriented principal component selection (FPCS) transformation (Crosta and Moore 1989) and analyses of contributions from each spectral band on principal components. Since alluvium contains hydroxyl and iron minerals, loadings from bands 1, 3, 5, and 7 representing wavelengths centered on 0.45, 0.67, 2.2, and 2.3 µm were studied, whereas the country rocks of the study area, such as sandstone, siltstone, limestone, and basalt, exhibit characteristic absorption features in longer-wavelength regions (8–12 µm) and do not interfere with spectral features of alluvium. In the second approach, field spectra representing alluvium were collected, resampled, and matched with image spectra using Spectral Angle Mapper (SAM) algorithm (Kruse et al. 1993). This technique directly maps the pixels that are similar to field spectra (Eq. 3) representing alluvium. Field spectra representing alluvium were collected from 15 sites (Fig. 3A) using a field-portable spectroradiometer (model SVC HR-1024). The instrument was calibrated using a white reference (spectralon panel). These spectra were subsequently resampled to Landsat bandwidth (Fig. 3B) using ENVI software.

$$\alpha = Cos^{-1}\left[\frac{\sum_{i}^{nb} t_i r_i}{\left(\sum_{i=1}^{nb} t_i^2\right)^{1/2}\left(\sum_{i=1}^{nb} r_i^2\right)^{1/2}}\right] \qquad (3)$$

where α is the angle between test and target spectra, t_i is the pixel spectrum, r_i is the reference spectrum, and nb is the number of bands.

3.2 Geotechnical studies

The failure vulnerability of alluvial area needs to be evaluated for seismic demand, resisting capacity and factor of safety. Failure demand is the load imparted to the soil by earthquake (in terms of both amplitude and duration). Capacity is the demand required to cause failure, and factor of safety is the ratio between the capacity and demand. Liquefaction and lateral spreading of saturated, unconsolidated sand, loam, and gravel occurs

when the demand is more than the capacity. Traditionally, failure vulnerability due to cyclic loading is evaluated based on sediment type, depth to water table, seismic load, and resistance of the soil (Seed et al. 1985). In this study, the vulnerability was evaluated from field data on cyclic stress ratio (CSR) and cyclic resistance ratio (CRR) based on the procedures outlined by Seed and Idriss (1971) and Youd et al. (2001). Seismic demand (CSR) was computed from the peak ground acceleration (PGA). Resistance to failure (CRR) of the foundation soil was evaluated using field data on standard penetration test (SPT), in situ density, and soil index properties (Seed et al. 1983, 1985). The above testing was carried out by following the Indian Standard procedures (IS: 2131-1981).

Standard penetration test (SPT) values are widely accepted as a robust technique in evaluating the resistance of soil to liquefaction (Seed et al. 1983, 1985). Thirteen shallow boreholes were made within the alluvial areas mapped using Landsat data. From borehole test, details on litholog, penetration resistance (SPT), fines content, and in situ density of the soils were generated (Table 1). The field SPT blow counts were normalized to overburden pressure of 100 kPa and hammer efficiency of 60 % $(N_1)_{60}$ by using Eq. 4 (Seed et al. 1983, 1985):

$$(N_1)_{60} = N_M * C_N * C_E * C_B * C_R * C_S \tag{4}$$

where

N_M—field-measured penetration resistance
C_N—$(Pa/\sigma'_{vo})^{0.5}$—factor to normalize overburden pressure
C_E—correction factor for hammer energy (0.90)
C_B—correction for borehole diameter
C_R—correction for rod length
C_S—correction for sampler

Since the fines content, F (<0.075 mm), increases the cohesion and decreases the penetration depth, resistance $(N_1)_{60}$ to penetration due to fines is corrected to arrive at "equivalent clean sand values" $(N_1)_{60cs}$ using the Eq. (5).

$$(N_1)_{60cs} = \alpha + \beta(N_1)_{60} \tag{5}$$

The coefficients α and β were estimated from the following relation:

$$\alpha = 0 \text{ for } F \leq 5 \quad \beta = 1.0 \text{ for } F \leq 5$$

$$\alpha = \exp\left[1.76 - \left(190/F^2\right)\right] \text{ for } 5 < F < 35$$
$$\beta = \left[0.99 + \left(F^{1.5}/1{,}000\right)\right] \text{ for } 5 < F < 35$$

$$\alpha = 5 \text{ for } F \geq 5 \quad \beta = 1.2 \text{ for } F \geq 5$$

The CRR and SPT correlation chart adjusted to magnitude of Bhuj earthquake (Mw = 7.7) by Krinitzsky and Hynes (2002) is used herein for analysis. The earthquake load measured through CSR (Eq. 6) was obtained from the simplified equation of Seed and Idriss (1971):

$$\text{CSR} = (\tau_{av}/\sigma'_{vo}) = 0.65(a_{max}/g)(\sigma_{vo}/\sigma'_{vo}) r_d \tag{6}$$

where

a_{max}—peak horizontal acceleration at ground surface
g—acceleration due to gravity
σ_{vo} σ'_{vo}—total and effective overburden stress, respectively

Table 1 Borehole data depicting the litholog and geotechnical attributes

Location	Sample No	Borehole lithology	Thickness (m)	Soil type	SPT ($N_{1,60}$)	Density (%)	WL above AMSL (m)
Madhapar Road	MR1	Silty sand	1	SP-SM	14	40	18.0
	MR2	Coarse sand with	4	SP	16	35	
	MR3	Pebbles					
	MR4	Silty sand with clay	2	SM	25	65	
North of Bhuj town	NB1	Bentonitic clay and sand	0.95	SM	15	30	17.4
	NB2	Weathered S.St.	2.00	N.A	49	95	
	NB3	S.St.	N.E	N.A	N.A	N.A.	
East of Bhuj town	EB1	Silty sand and coarse sand.	1	SM	11	33	22.5
	EB2	Coarse sand	2	SP	12	37	
	EB3	Medium–fine sand	2	SP	24	60	
Airport	BA1	Coarse sand with clay	0.6	SP-SC	12	25	12.0
	BA2	Sand with clay	1.2	SP	32	65	
	BA3	Coarse sand	5	SP	39	60	
Rawal Wadi	RW1	Silty sand	2	SM	16	42	19.4
	RW2	Coarse sand	2	SP	7	23	
	RW3	Coarse sand with clays	4	SP-SC	45	87	
Haripar Road	HR1	Coarse sand with silt	0.8	SP	15	56	30.0
	HR2	Fine sand with silt	2	SM	21	37	
	HR3	Coarse sand with clay	3	SP	30	68	
Central School	BCS1	Silty sand	1	SM	24	46	25.0
	BCS2	Coarse sand with silt	1	SP	24	68	
		Weathered S.St	N.E	N.A	39	84	
Ghenla	GN1	Coarse sand with clay	0.9	SP-SC	10	32	13.2
	GN2	Fine sand with silt	1	SP	15	47	
	GN3	Gravel	4	SP	29	55	
	GN4	Coarse sand Weathered S.St	N.E	NA	36	85	
Airport road	BAR1	Coarse sand with clay	1	SP-SC	12	30	21.0
	BAR2	Silty sand	2	SM	26	57	
	BAR3	Sand with clays	1	SP	23	40	
	BAR4	Clayey sand	5	SC	17	67	

S.St. sandstone, *N.A.* not available, *RWL* reduced water level, *N.E* not estimated (after Ramakrishnan et al. (2006))

r_d—stress reduction coefficient estimated from
r_d -1.0-0.00765 Z for depth (Z) ≤ 9.15 m.

The maximum-recorded peak ground acceleration (PGA) for 2001 event (0.38) was used to estimate CSR values. Since saturation is one of the important criteria in pore pressure buildup, depth to reduced water level was collected from 40 wells located within

the alluvium and subsequently groundwater contours were constructed. Finally, spatial and attribute data such as distribution of alluvium, factor of safety, and water table were integrated using GIS (ARC/Info ver. 9.0). The schema of steps followed is illustrated in the flowchart (Fig. 2).

4 Results

4.1 Mapping the alluvial areas

Alluvium of the investigated area predominantly comprises quartz, hydroxyl-bearing minerals, and iron hydroxides. An abundance of clays (kaolin, illite, montmorillonite) and sheet silicates in the alluvium indicate absorption in 2.1–2.4 µm range (band 7) due to molecular vibration processes. Similarly, the presence of iron oxides/hydroxides (such as hematite and goethite) in the alluvium is expected to exhibit strong absorption in the blue region (band 1) and higher reflectance in red region (band 3) due to charge-transfer effect. The field spectra of the alluvial soils representing loamy sand and sandy loam (Fig. 3A) also reflect the presence of these mineral phases.

It is evident from the principal component transformation (Table 2) that the first principal component (comprising 82.38 % of the variance of six bands) contains information mainly on albedo and topography. Vegetation is enhanced in PC3 as this PC has higher loading of band 4 (0.63). PC4 is observed to enhance the hydroxyl minerals with higher loadings of bands 5 (0.63) and 7 (−0.69). The clay minerals have absorption in band 7 and reflection in band 5, and hence, PC4 with a positive contribution of band 5 and negative contribution of band 7 is in perfect agreement with spectral characters of the soils. Using this loading information, a hydroxyl image was generated using Eq. (7).

$$PC4 = 0.27(Band\ 1) + 0.17(Band\ 2) - 0.10(Band\ 3) - 0.16(Band\ 4)$$
$$+ 0.63(Band\ 5) - 0.69(Band\ 7) \qquad (7)$$

The above equation is expected to render pixels with clay mineral to appear bright. Accordingly, the resultant image was density sliced to demarcate the regions of higher reflectance (0.61–0.62) representing alluvial areas. Similarly in PC5, significant
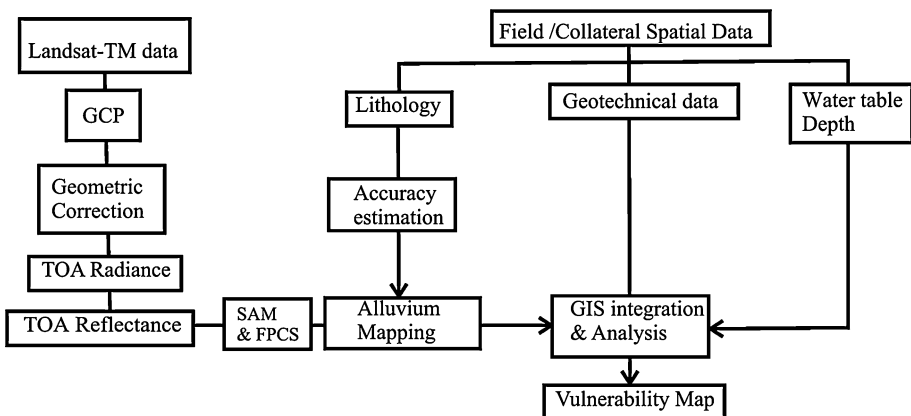

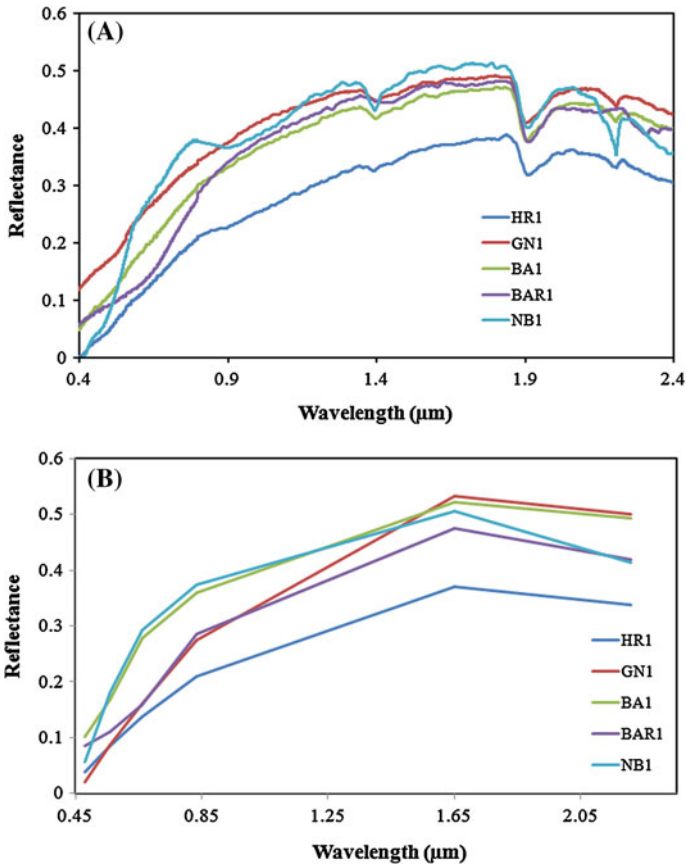Fig. 2 Flowchart depicting the adopted methodology

Fig. 3 Stacked field spectra (offset = 0.1) of alluvial soils indicating the abundance of iron and clay (**A**), and field spectra resampled to Landsat-TM bandwidth (**B**)

contributions from band 1 (−0.72) and band 3 (0.56) (Eq. 8) were observed. Since loading from band 3 is lower than from band-1, regions rich in iron oxides/hydroxides are expected to appear darker. Density slicing of PC5 with a threshold of 0.01–0.02 resulted in mapping the iron-rich alluvial regions.

$$
\begin{aligned}
PC5 = {} & -0.73(\text{Band 1}) - 0.21(\text{Band 2}) + 0.56\,(\text{Band 3}) + 0.04\,(\text{Band 4}) \\
& + 0.13\,(\text{Band 5}) - 0.30\,(\text{Band 6})
\end{aligned}
\tag{8}
$$

The above two density-sliced raster images were subsequently converted to vector layers and intersected in GIS to generate a single composite map (Fig. 4A). It is evident from Fig. 4A that the adopted procedure was effective in delineating present and paleo-river channels, flood plains, fan deposits, and colluvial areas.

For target mapping using SAM technique, resampled field spectra and atmospherically corrected TM data were used. The threshold values of mapping were progressively increased from 0.1 to 0.4, and each time, the classified output was compared with field data for accuracy. When maximum classification accuracy (87 %) was achieved (for alluvium) with a threshold of 0.22, the classification (Fig. 4B) was considered satisfactory. The

Table 2 Principal components of six ETM+ bands of Bhuj area

	PC1	PC2	PC3	PC4	PC5	PC6
Band 1	0.176	−0.208	−0.277	0.268	−0.727	−0.497
Band 2	0.264	−0.267	−0.371	0.167	−0.206	0.805
Band 3	0.480	−0.464	−0.356	−0.096	0.564	−0.312
Band 4	0.143	0.743	−0.630	−0.159	0.036	−0.048
Band 5	0.576	0.336	0.377	0.627	0.131	−0.001
Band 7	0.560	0.053	0.342	−0.686	−0.302	0.057
Covariance eigenvalue	3620.54	411.37	312.29	26.95	19.17	4.36
Percentage of variance	82.38	9.36	7.10	0.61	0.43	0.01

confusion matrix (Table 3) generated based on field data from 35 locations indicates that classification accuracy for Younger alluvium is the highest (87 %) followed by Older alluvium (67 %). Lower accuracy of unclassified pixels (50 %) further supports the efficacy of delineation of alluvium. From Table 3 and Fig. 4A, B, it is evident that the results of SAM and FPCS are comparable. Finally, SAM and FPCS classification results were intersected in GIS. From the resultant coverage, polygons that were classified as alluvium by both FPCS and SAM techniques were identified to generate composite alluvium map (Fig. 5).

4.2 Evaluation of liquefaction susceptibility

From the field investigations, it is evident that the study area consists of unconsolidated sediments distributed along Younger and Older alluvial plains, fan deposits, and tidal flats. The northern parts of the Bhuj city (airport and surrounding area) comprise the Younger and Older alluvia and weathered sandstones. From the borehole records, it is obvious that the unconsolidated sediments are predominantly sandy with several intercalated layers of clay and loam (Table 2) having thickness from 2 to 20 m. Laterally, these sediments have limited continuity. Besides these rock types, occasional exposures of shale, basaltic flows, and basic dykes are also found. Based on geology, three failure vulnerability classes were evolved, namely *high* (which includes unconsolidated Younger alluviums, flood plain deposits, paleo-channels, alluvial fans, and the bajada/colluvial materials with effluent conditions), *medium* (poorly consolidated alluviums and weathered sandstones), and *low* (well-consolidated sedimentary rocks) classes.

The CSR and CRR values of alluvial soils estimated during this investigation and reported by others (Table 4) indicate that the unconsolidated sediments of the investigated area can undergo liquefaction for PGA values starting from 0.24 g. Based on factor of safety, the area is classified into three vulnerability classes, namely *high* (Fs ≤ 0.9), *medium* (Fs = 0.9–1.1), and *low* (Fs > 1.1).

As saturation is an important criterion for pore pressure buildup, depth to reduced water table from several locations was collected from the field and contoured. In general, depth to water table varied from 0.2 to 30 m. Besides regional water table, fully saturated perched aquifers are also evidenced at many places. These aquifers augment the scope for liquefaction, and their spatial distribution is difficult to map. Based on the depth to water table, the study area is grouped into three classes, namely *high* (<6 m)-, *medium* (6–15 m)-, and *low* (>15 m)-susceptible classes.
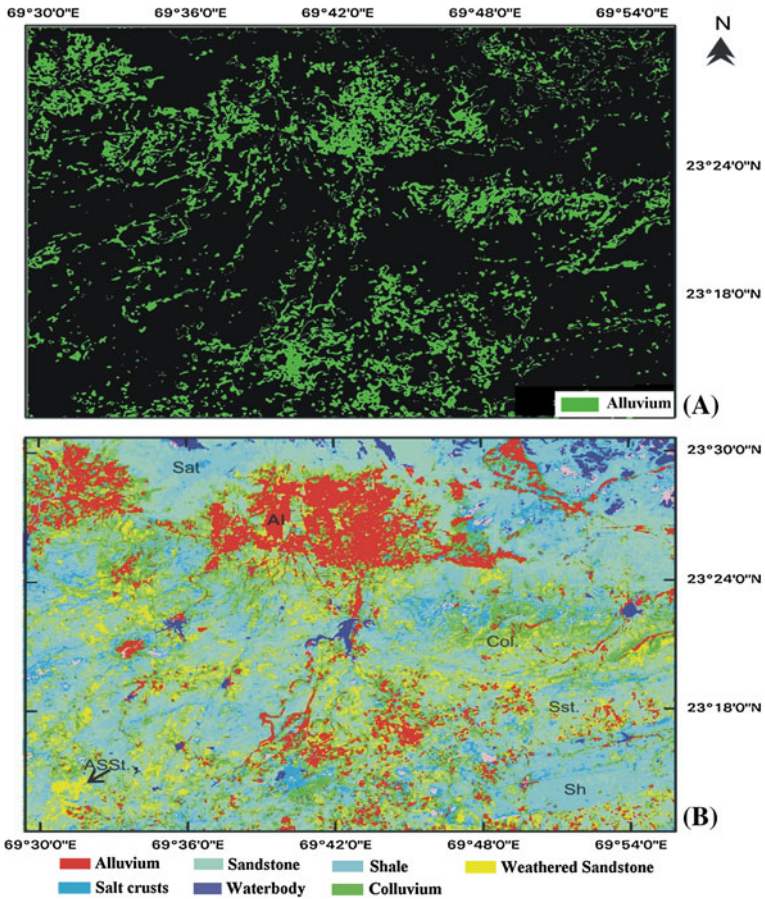
Fig. 4 (**A**) Alluvium distribution map derived by FPCA technique. (**B**) Distribution of alluvium mapped using field spectra and SAM technique

4.3 GIS analysis

The spatial database on alluvium distribution, depth to water table, and factor of safety was integrated in GIS (ARC/Info), and overlay analysis was carried out to derive a final hazard potential map (Fig. 6). Four hazard potential classes, namely *high*, *moderate*, *low*, and *not susceptible*, were identified based on the following decision rules.

High-susceptibility areas: Areas with unconsolidated sediments (Younger alluvium) having Fs <1.0 and depth to water table less than 6 m.
Moderate-susceptibility areas: Areas comprising unconsolidated sediments (Younger alluvium) having Fs = 0.9–1.0 and depth to water table between 6 and 15 m.
Low-susceptibility areas: Areas with unconsolidated and poorly consolidated sediments (Older alluvium) having Fs = 0.9–1.0 and depth to water table 6–15 m.
Not susceptible areas: Areas that comprise consolidated rocks, poorly consolidated sediments having Fs > 1.0, and depth to water table >15 m.

Table 3 Confusion matrix indicating the classification accuracy by SAM and FPCS techniques

| A. Classification by SAM technique					Total samples	Users' accuracy (%)
	Younger Alluvium	Older Alluviums	Bazada	Unclassified (country rocks)		
Younger alluvium	13	03	00	00	16	81
Older alluviums	02	06	00	01	09	67
Bazada	00	00	05	01	06	83
Country rocks	00	00	02	02	04	50
Total samples	15	09	07	04	35	
Producers' accuracy (%)	87	67	71	50		
B. Classification by FPCS technique						
Younger alluvium	14	02	00	00	16	87
Older alluviums	05	04	00	00	09	44
Bazada	00	01	04	01	06	67
Country rocks	00	00	02	02	04	50
Total samples	19	07	06	03	35	
Producers' accuracy (%)	73	57	67	67		
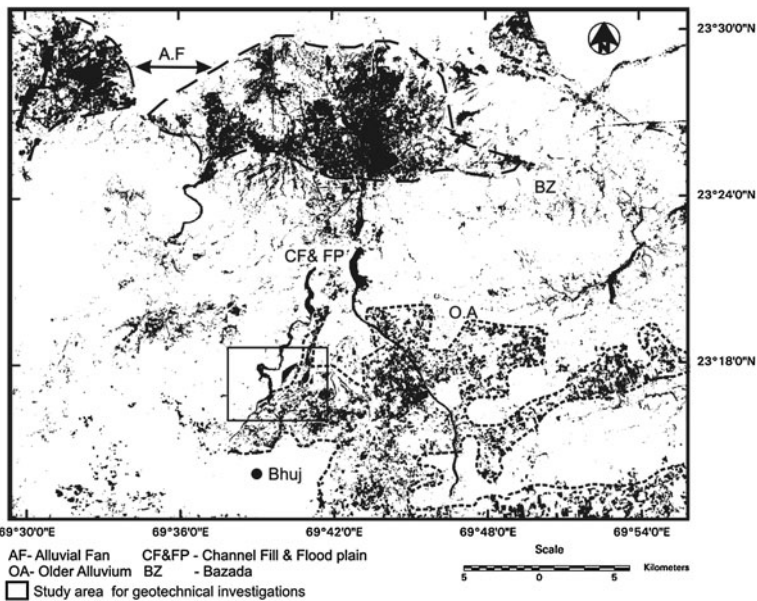
Fig. 5 Composite map indicating distribution of unconsolidated sediments in and around Bhuj

5 Discussion and conclusions

Ramakrishnan et al. (2006), demonstrated the utility of remote sensing in identification of ground deformation after a seismic event. This paper is based on a new approach wherein the recent sediments are identified and mapped based on spectral characters of

Table 4 Derived liquefaction susceptibility conditions of foundation soils

Locations	CRR	CSR	Factor of safety	Liquefaction susceptibility
Madhapar road*	0.22	0.25	0.88	Yes
North of Bhuj town*	0.25	0.23	1.08	Marginal
East of Bhuj town	0.38	0.26	1.46	No
Airport*	0.22	0.23	0.95	Yes
Rawal Wadi*	0.22	0.23	0.95	Yes
Haripar road*	0.32	0.25	1.28	No
Central School*	0.27	0.24	1.12	Marginal
Ghenla*	0.33	0.25	1.32	No
Airport road*	0.21	0.23	0.91	Yes
Chang Dam#				
Crest	0.32	0.35	0.91	Yes
Toe	0.32	0.73	0.43	Yes
Tapar Dam[#]				
Crest	0.32	0.30	1.06	Marginal
Toe	0.32	0.62	0.52	Yes
Fatehgadh Dam[#]	0.32	0.18	1.78	No
Crest	0.32	0.35	0.91	Yes
Toe				
Kaswati Dam[#]				
Crest	0.32	0.17	1.89	No
Toe	0.32	0.34	0.94	Yes
Shivlakha Dam[#]				
Crest	0.32	0.31	1.03	Marginal
Toe	0.32	0.63	0.51	Yes

[#] Compiled after Singh et al. (2005) and

* modified after Ramakrishnan et al. (2006)

unconsolidated sediments associated with recent/paleo-channels, flood plains, and fan deposits. For this purpose, Landsat-TM data having bands in visible, near-, and short-wave infrared region was used in conjunction with field reflectance spectra. Since the alluvial sediments comprise quartz, clay, and iron hydroxides (Fig 3A), their reflectance spectra contain characteristic absorption features centered on 0.5-, 2.2-, 2.3-, and 2.4-μm wavelength regions. Accordingly, pixels representing the alluvium are also expected to show absorptions in these wavelengths. To map the pixels showing these characters, SAM and FPCS algorithms were used. From the results, it is evident that both techniques efficiently delineated the alluvium. From field observations made at 40 locations, it was observed that the alluvium mapped is reasonably (87 %) accurate. Subsequently, field geotechnical investigations were carried out at representative sites to evaluate the resistance (CRR) of these soils for liquefaction using SPT tests. It is clear from Table 4 that the factors of safety of the alluvial soils range from 0.88 to 1.8 for the 2001 seismic event with PGA 0.38. Considering the past episodes of major earthquakes in this region (e.g., 1819 earthquake with 8.2 magnitude), these alluvial soils warrant further investigation for its performance under higher seismic demand.
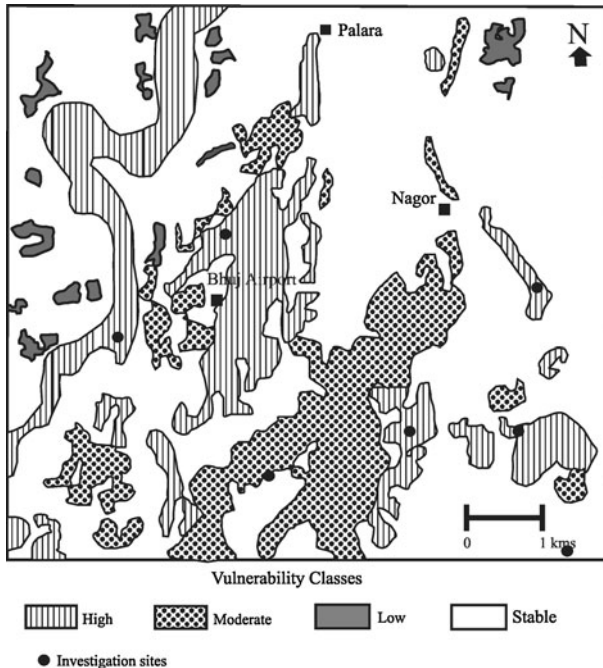
Fig. 6 Map showing the liquefaction-susceptible areas in and around Bhuj

Finally, based on the liquefaction susceptibility for the given parameters such as extent of consolidation, Fs, and depth to water table, the map was classified into four classes, namely high-, moderate-, low-, and not susceptible classes. Further, the derived susceptibility classes commensurate well with the observed (Ramakrishnan et al. 2006) liquefaction severity (R^2 = 0.97) for 2001 event. Thus, this study illustrates the efficacy of remote sensing, GIS, and geotechnical techniques for rapid and effective mapping of potential ground failure zones in seismically active areas.

References

Abrams MJ, Brown D, Lepley L, Sadowski R (1983) Remote sensing for porphyry copper deposits in Southern Arizona. Econ Geol 78:591–604

Amos BJ, Greenbaum D (1989) Alteration detection using TM imagery: the effects of supergene weathering in arid climate. Int J Remote Sens 10:515–527

Biswas SK, Khattri KN (2002) Geologic study of earthquake in Kutch, Gujarat, India. J Geol Soc India 60:131–142

Buckingham WF, Sommer SE (1983) Mineralogical characterization of rock surfaces formed by hydrothermal alteration and weathering—application to remote sensing. Econ Geol 78:664–674

Chander G, Markham B (2003) Revised Landsat-5 TM Radiometric Calibration procedures and post calibration dynamic ranges. IEEE Trans Geosci Remote Sens 41:2674–2677

Chavez P Jr (1996) Image-based atmospheric corrections- Revisited and improved. Photogramm Eng Remote Sensing 62:1025–1036

Chu BL, Hsu SC, Chang YM (2003) Ground behavior and liquefaction analyses in central Taiwan-Wufeng. Eng Geol 71:119–139

Crosta AP, Moore JM (1989) Enhancement of Landsat Thematic Mapper imagery for residual soil mapping in SW Minais Gerais State, Brazil: a prospecting case history in Greenstone belt terrain. Proceedings of the 7th (ERIM) Thematic Conference, Remote Sensing for Exploration Geology: 1173–1187

Davis RO, Berrill JB (1982) Energy dissipation and seismic liquefaction in sands. Earthq Eng Struct Dynam 10(1):59–68

Dobry R, Ladd RS, Yokel FY, Chung RM, Powell D (1982) Prediction of pore water pressure buildup and liquefaction of sands during earthquakes by the cyclic strain method. U.S. Natl Bureau Stand 138:1–150

Franck AAM, Carlos Go′mez TJ, Tavera HJ, Orihuela NG (2005) Soil liquefaction during the Arequipa Mw 8.4, June 23, 2001 earthquake, southern coastal Peru. Eng Geol 78:237–255

Green RA, Mitchell JK (2004) Energy-based evaluation and remediation of liquefiable soils. Geotechnical Engineering for Transportation Projects (M. Yegian and E. Kavazanjian, ed.), ASCE Geotechnical Special Publication 126(2): 1961–1970

Gupta RP, Saraf AK, Chander R (1998) Discrimination of areas susceptible to earthquake-induced liquefaction from Landsat data. Int J Remote Sens 19:569–572

Haiming Y, Susan HY, Andrus RD, Juang CH (2004) Liquefaction-induced ground failure: a study of the Chi-Chi earthquake cases. Eng Geol 71(1–2):141–155

Ishihara K (1993) Liquefaction and flow failure during earthquakes. Géotechnique 43(3):351–415

Ishitsuka K, Tsuji T, Matsuoka T (2012) Surface change of the soil liquefaction caused by the 2011 great east Japan earthquake derived from SAR data. Proc. Intl. Symp. on Engineering Lessons learned from the (2011) Great East Japan Earthquake, March 2012. Tokyo, Japan, pp 849–854

Iyengar RN, Raghukanth STG (2002) Strong Ground motion at Bhuj city during the Kutch Earthquake. Curr Sci 82(11):1366–1372

Kaufman H (1988) Mineral exploration along the Aqaba-Levanat structure by use of TM data, concepts, processing and results. Int J Remote Sens 9:1630–1658

Kayen RE, Mitchell JK (1997) Assessment of liquefaction potential during earthquakes by Arias intensity. J Geotech Geoenviron Eng, ASCE 123(12):1162–1174

Krinitzsky EL, Hynes ME (2002) The Bhuj, India earthquake: lessons learnt for earthquake safety of dams on alluvium. Eng Geol 66:163–196

Kruse FA, Lefkoff AB, Boardman JB, Heidebrecht KB, Shapiro AT, Barloon PJ, Goetz AFH (1993) The spectral image processing system (SIPS)—interactive visualization and analysis of imaging spectrometer data. Remote Sens Environ 44:145–163

Liang S (2001) Atmospheric correction of Landsat ETM+ land surface imagery—part-1: methods. IEEE trans Geosci Remote Sens 39(11):2490–2498

Leea DH, Kub Chih-Sheng, Yuanc H (2003) A study of the liquefaction risk potential at Yuanlin, Taiwan. Eng Geol 71:97–117

Oommen T, Baise LG (2008) A new approach to liquefaction potential mapping using remote sensing and machine learning. Proc. IEEE International Conference on Geoscience and Remote Sensing Symposium, July 2008, Boston, USA, 3: 51–54

Orense RP, Pender MJ, Wotherspoon LM (2012) Analysis of soil liquefaction during the Recent Canterbury (New Zealand) Earthquakes. Geotech Eng J SEAGS & AGSSEA 43(2):8–17

Rajendran K, Rajendran CP, Thakkar M, Tuttle MP (2001) The 2001 Kutch (Bhuj) Earthquake: coseismic surface features and their significance. Curr Sci 80:1397–1405

Ramakrishnan D, Mohanty KK, Nayak SR, Vinu Chandran R (2006) Mapping the liquefaction induced soil moisture changes using remote sensing technique: an attempt to map the earthquake induced liquefaction around Bhuj, Gujarat, India, Jour. Geotech Geol Eng 24:1581–1602

Sahoo RN, Reddy DV, Sukhija BS (2007) Evidence of liquefaction near Baramulla (Jammu and Kashmir, India) due to the 2005 Kashmir earthquake. Curr Sci 92(3):293–295

Saito K, Spence RJS, Going C, Markus M (2004) Using high-resolution satellite images for post earthquake building damage assessment: a study following the 26.1.01 Gujarat earthquake. Earthq Spectra 20(1):145–169

Saraf AK, Sinvhal A, Sinvhal H, Ghosh P, Sarma B (2002) Satellite data reveals 26 January 2001 Kutch Earthquake induced ground changes and appearance of water bodies. Int J Remote Sens 23(9):1749–1756

Seed HB, Idriss IM (1971) Simplified procedure for evaluating soil liquefaction potential. J Soil Mech Found Div, ASCE 97:1249–1273

Seed HB, Idriss IM, Arango I (1983) Evaluation of liquefaction potential using field performance data. J Geotech Eng, ASCE 109:458–482

Seed HB, Tokimatsu K, Harder L, Chung R (1985) Influence of SPT procedures. in soil liquefaction resistance evaluations. Jour. Geotech Eng, ASCE 111:1425–1445

Singh RP, Bhoi S, Sahoo AK (2001) Changes observed in land and ocean after Gujarat earthquake of 26 January 2001 using IRS data. Int J Remote Sens 23(16):3123–3128

Singh R, Roy D, Jain SK (2005) Analysis of earth dams affected by the 2001 Bhuj Earthquake. Eng Geol 80:282–291

Tangestani MH, Moore F (2001) Comparison of three principal component analysis techniques to porphyry copper alteration mapping. A case study, Meiduk area, Kerman, Iran. Can J Remote Sens 27:176–182

Thomas L, Holzer TL, Bennett MJ, Ponti DJ, Tinsley JC (1999) Liquefaction and soil failure during 1994 Northridge earthquake. J Geotech Geoenvironment Eng 125(6):438–452

Tuttle MP, Hengesh JV (2002) Liquefaction. In: Bhuj, India earthquake of January 26, 2001 reconnaissance report.(Jain SK, Lettis WL, Murty CVR and Barder JP Eds.). Earthquake Spectra 18: 79–100

Van der Meer F, Vazquez-Torres M, Van Dijk PM (1997) Spectral characterization of ophiolite lithologies in the Troodos Ophiolite complex of Cyprus and its potential in prospecting for massive sulphide deposits. Int J Remote Sensing 18:1245–1257

Verdugo R, Sitar N, Frost JD, Bray JD, Candia G, Elridge T, Hashash Y, Olson SM, Urzua A (2012) Seismic performance of earth structures during the February 2010 Maule, Chile Earthquake: Dams, Levees, Tailings Dams and Retaining walls. Earthq Spectra 28(S1):S75–S96

Whitman RV (1971) Resistance of soil to liquefaction and settlement. Soils Found 11(4):59–68

Youd TL (1991) Mapping of earthquake induced liquefaction for seismic zonation. Proc. 4th Intl. Conf. On Seismic Zonation, Standford, Califor. 111–147

Youd TL, Keefer DK (1981) Earthquake induced ground failures in facing geologic and hydrologic hazards. U.S. Geological Survey professional paper 1240-B: 23–31

Youd TL, Perkins DM (1987) Mapping of liquefaction severity index. J Geotech Eng, ASCE 113:1374–1392

Youd TL, Idriss IM, Andrus RD, Arango I, Castro G, Christian JT, Dobry R, LiamFinn WD, Harder LF Jr, Hynes ME, Ishihara K, Koester JP, Laio SSC, Marcuson WF III, Martin GR, Mitchell JK, Moriwaki Y, Power MS, Robertson PK, Seed RB, Stokoe KH II (2001) Liquefaction resistance of soils. Summary report from the 1996 NCEER and 1998 NCEER/NSF workshops on evaluation of liquefaction resistance of soils. J Geotech Geoenviron Eng 127:817–833

Yuan H, Susan HY, Ronald DA, Juang H (2003) Liquefaction induced ground failure: a study of the Chi-Chi earthquake cases. Eng Geol 17:141–155